Polarization attractors driven by vector soliton rain

SERGEY V. SERGEYEV,[*] [iD] **MAHMOUD ELIWA, AND HANI KBASHI**

Aston Institute of Photonic Technologies, Aston University, Birmingham B4 7ET, UK
[*]*s.sergeyev@aston.ac.uk*

Abstract: Soliton rain is a bunch of small soliton pulses slowly drifting near the main pulse having the period of a round trip. For Er-doped fiber laser mode-locked by carbon nanotubes, for the first time, we demonstrate both experimentally and theoretically a new type of polarization attractors controllable by vector soliton rain. With adjusting the pump power, vector soliton rain takes the form of pulses with rotating states of polarization which enable transforming slowly evolving trajectories on the Poincaré sphere from the double-scroll spiral to the circle. The obtained results on controlling complex multisoliton dynamics can be of interest in laser physics and engineering with potential applications in spectroscopy, metrology, and biomedical diagnostics.

1. Introduction

Mode-locked laser (MLL) as a testbed for generating the dissipative solitons (DSs) with controllable parameters is widely used to study short-range and long-range interactions among DSs in the context of unlocking the routes to control the formation of self-stabilized structures in a wide range of distributed systems [1–17]. Short-range interaction through the overlapping of solitons tails or soliton-dispersive wave interaction results in soliton bound states formation with the spacing of the few pulse widths [4–6]. Unlike this, long-range interactions can be driven, for example, by Casimir-like [7,8], optoacoustic [1–3], and polarization effects [9] and can lead to soliton supramolecular structures in the form of multi-pulsing, harmonic mode-locking, breather-like, and the soliton rain (SR) [1–3,8–14]. The absence of effective approaches to controlling long-range soliton interactions leads to harmonically mode-locked laser pulses with uncontrollable repetition rates and high timing jitter, drifting soliton rain, or weakly-bound solitons (see references in [15]). The most effective approach for control is based on tailoring optoacoustic effects and dispersive-wave emission. As a result, it was demonstrated that the self-assembly of the optical solitons into stable supramolecular structures can find potential applications in optical information storage and ultrafast laser dynamic waveforms manipulation [15].

The supramolecule in the form of SR presents a bunch of small soliton pulses located nearby the main pulse and coexisting with a continuous wave (cw) background [8–13]. The soliton rain was studied experimentally and theoretically for fiber lasers with different mode-locking mechanisms based on nonlinear polarization rotation (NPR), nonlinear amplified loop mirror (NALM), the figure of eight cavity, graphene, and single-wall carbon nanotubes (SWCNT) [8–13]. Though the variety of mechanisms of SR evolution in different MLLs has been studied in detail, the effective approaches to control the SR have not been revealed yet. In our previous work [9], we found competition between polarization hole burning induced by SR and hole refilling driven by the pump wave, and the state of polarization (SOP) evolution can drive the SR dynamics towards SR pulses merging or repulsing. However, observed fast polarization dynamics and low

temporal resolution of polarimeter were obstacles to revealing complex polarization attractors on the Poincaré sphere and so to conclude about approaches to control SR emergence.

Here, we report for the first time the experimental and theoretical results on the polarization attractors mediated by the soliton rain evolution in the laser cavity. The soliton rain dynamics in the fast time scale of the nanosecond range were analyzed by using a fast photodetector and oscilloscope. The slow vector dynamics in the time scale of microseconds was studied by using an in-line polarimeter. To explain the tunability of polarization attractors from the double-scroll spiral to the circle on the Poincaré sphere, a new theoretical model was developed. In this model, the vector SR was presented in the form of the injected signal with rotating states of polarization, increased amplitude of which leads to the attractor's tunability close to the experimentally observed.

2. Experimental setup and methods

The schematic of the unidirectional cavity fiber laser mode-locked is shown in Fig. 1. It has a 14 m long ring cavity corresponding to a round trip time of 70 ns and so the fundamental frequency of mode-locked oscillations is 14.28 MHz. The cavity consists of 13 m standard single-mode optical fiber (SMF-28) with $\beta_2 = -22 \ ps^2 km^{-1}$ and a 1 m long erbium-doped fiber (EDF: Liekki Er80-8/125) with the absorption of 80 dBm^{-1} at 1530 nm acting as the gain medium. The EDF is pumped with a 980 nm laser diode (LD) followed by a polarization controller (PC) to adjust the pump light ellipticity. A 980/1550 nm wavelength-division multiplexer (WDM) is used to couple the pump light into the laser cavity. A polarization-independent optical isolator with attenuation of 51 dB is incorporated into the cavity to force the unidirectional operation of the laser. A carbon nanotube (CNT) is used as a saturable absorber to initiate the mode-locking regime, followed by a second PC to tune the linear and circular cavity birefringence. A 90/10 fiber coupler is used to feedback 90% to the laser cavity, and 10% is extracted as the output signal. Instead of using the general approach of splicing fiber to form the ring cavity, all the components are attached through APC fiber connectors. The signal was detected by using a photodetector with a bandwidth of 17 GHz (InGaAsUDP-15-IR-2 FC) connected to a 2.5 GHz sampling oscilloscope (Tektronix DPO7254). An in-line polarimeter (Thorlabs IPM5300) with the resolution of 1 ∓s and recorded 1024 samples was used to record the state and degree of polarization (SOP and DOP), respectively.
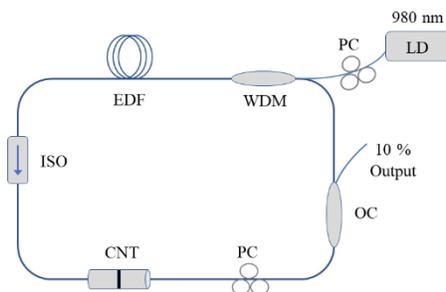

Fig. 1. Erbium-doped fiber laser. EDF: erbium-doped fiber; LD: 980 nm laser diode for the pump; PC: polarization controllers, ISO: optical isolator; WDM: wavelength division multiplexer (WDM), OC: 90:10 output coupler.

3. Experimental results

The results on the fast dynamics are shown in Figs. 2(a)-(f). The results have been obtained without adjustment of polarization controllers and with changing pump power as follows: P = 114

mW (a), (d), 108 mW (b), (e), and 148 mW (c), (f). As follows from Fig. 2, the soliton rain changes shape from the condensed phase (Figs. 2(a), (b)) to the bunch of pulses like a burst of soliton rain shown in Fig. 2(c). As follows from Figs. 2(d)-(f), transition to the burst is accompanied by the emergence of the cw component in Fig. 2(f).
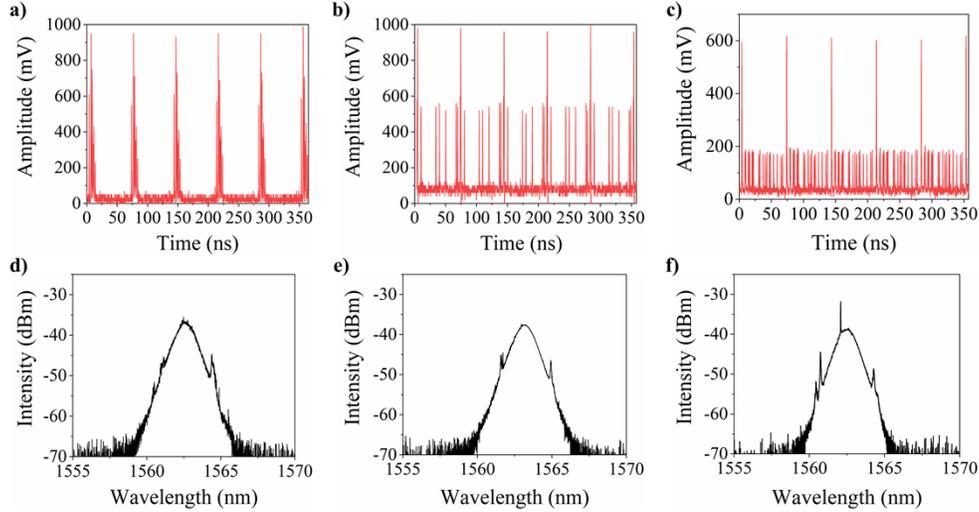
Fig. 2. Fast dynamics. Oscillograms (a)-(c), and corresponding optical spectra (d)-(f). Parameters: Pump current P = 114 mW (a), (d); 108 mW (b), (e); 148 mW (c), (f).

To study the soliton rain pulses' effect on the state of polarization, we use a polarimeter (resolution of 1 μs and recorded 1024 samples) to measure the normalized Stokes parameters s_1, s_2, s_3, and degree of polarization (DOP) which are related to the output powers of two linearly cross-polarized SOPs I_x and I_y and phase difference between them $\Delta\phi$ as follows:

$$S_0 = I_x + I_y, \ S_1 = I_x - I_y, \ S_2 = 2\sqrt{I_xI_y}\cos\varDelta\phi, \ S_3 = 2\sqrt{I_xI_y}\sin\varDelta\phi,$$

$$s_i = S_i/\sqrt{S_1^2 + S_2^2 + S_3^2}, \quad DOP = \sqrt{S_1^2 + S_2^2 + S_3^2}/S_0, (i = 1, 2, 3). \tag{1}$$

The obtained results are shown in Figs. 3(a)-(i). The slow dynamics corresponds to the cases of the dynamics shown in Fig. 2, i.e., Figs. 3(a), (d), (g) – to Figs. 2(a), (d), Figs. 3(b), (e), (h) – to Figs. 2(b), (e), and Figs. 3(c), (f), (i) – to Figs. 2(c), (f). For the case of the soliton rain condensed phase (Figs. 2(a), (d)), polarization dynamics is shown in Figs. 3(a), (d), g. As follows from Figs. 3(a), (b) and our previous publications, spiral attractors can emerge when the in-cavity birefringence is suppressed and the pump wave ellipticity is close to one [16–18]. The specific feature of the spiral attractor is antiphase dynamics of the orthogonal linearly polarized SOPs x and y shown accompanied by switching in Fig. 3(d) [16–18]. As shown in Fig. 3(g), the phase difference demonstrates the oscillations and phase slips between states of π/2 and 3π/2. The high DOP of about 90% indicates that polarization evolution is relatively slow and can be mapped with 1 μs resolution (Fig. 3(g)). If satellite pulses are located close to the main pulse (Figs. 2(b), (e)), the polarization dynamics (Figs. 3(b), (e), (h)) looks quite similar to the dynamics shown in Figs. 3(a), (d), (g). The main difference is in the oscillatory switching between x and y SOPs (Fig. 3(e) leading to the slight modification of the spiral attractor in Fig. 3(b) and oscillatory type of the phase slips in Fig. 3(h). The dropped DOP to 80% indicates that dynamics is faster than 1 μs. With the increased number of satellite pulses (Figs. 2(c), (f)), polarization attractor changes shape from spiral to circle, as shown in Fig. 3(c). The dynamics of x and y SOP takes the antiphase form shown in Fig. 3(f). The phase difference dynamics demonstrates oscillatory

behavior between states of $\pi/2$ and $3\pi/2$ (Fig. 3(i)). The high DOP of 95% is an indication of slow dynamics that can be mapped with a resolution of 1 µs (Fig. 3(i)).

4. Theoretical results

To understand the mechanism of polarization attractor evolution caused by drifting soliton rain, we developed a new vector model of EDFLs from the vector theory developed by Sergeyev and co-workers [1,16–18]. The model accounts for the linear and circular birefringence and evolution of the laser SOPs and the first excited level population in Er^{3+} doped active medium. The previous model was complemented by the model of the vector soliton rain in the form of an injected signal with periodically evolving orthogonal states of polarization:

$$E_x = a \cdot \cos(\Omega t + \phi_0), \; E_y = a \cdot \sin(\Omega t + \phi_0) \cdot exp(\Delta\varphi). \tag{2}$$

Here a is the amplitude of the soliton rain, Ω is the frequency of oscillations, and ϕ_0 is the initial phase, $\Delta\varphi$ is the phase difference between the orthogonal SOPs. The model is inspired by the idea that the main pulse produces the polarization hole burning in the orientation distribution of inversion and so SR pulses have SOPs different from the main pulse's SOP [18]. Periodically evolving SOP of the main pulse leads to the oscillation of the SR SOP as shown in Eq. (2). With taking into account Eq. (2), the model found in [1,16–18] can be presented as follows:

$$
\begin{aligned}
\frac{du}{dt} &= i\beta u + i\frac{\gamma}{2}\left(|u|^2 u + \frac{2}{3}|v|^2 u + \frac{1}{3}v^2 u^*\right) + D_{xx}u + D_{xy}v + E_x, \\
\frac{dv}{dt} &= -i\beta v + i\frac{\gamma}{2}\left(|v|^2 v + \frac{2}{3}|u|^2 v + \frac{1}{3}u^2 v^*\right) + D_{xy}u + D_{yy}v + E_y, \\
\frac{dn_0}{dt} &= \varepsilon\left[I_p + 2R_{10} - \left(1 + \frac{I_p}{2} + \chi R_{10}\right)n_0 - \chi R_{11}n_{12} - \chi n_{22}R_{12}\right], \\
\frac{dn_{12}}{dt} &= \varepsilon\left[\frac{(1-\delta^2)}{(1+\delta^2)}\frac{I_p}{2} + R_{11} - \left(1 + \frac{I_p}{2} + \chi R_{10}\right)n_{12} - \left(\frac{(1-\delta^2)}{(1+\delta^2)}\frac{I_p}{2} + \chi R_{11}\right)\frac{n_0}{2}\right], \\
\frac{dn_{22}}{dt_s} &= \varepsilon\left[R_{12} - \left(1 + \frac{I_p}{2} + \chi R_{10}\right)n_{22} - \chi R_{12}\frac{n_0}{2}\right], \\
R_{10} &= \frac{1}{(1+\Delta^2)}(|u|^2 + |v|^2), \quad R_{11} = \frac{1}{(1+\Delta^2)}(|u|^2 - |v|^2), R_{12} = \frac{1}{(1+\Delta^2)}(uv^* + vu^*).
\end{aligned}
\tag{3}
$$

Coefficients D_{ij} can be found as follows:

$$
\begin{aligned}
D_{xx} &= \frac{\alpha_1(1-i\Delta)}{1+\Delta^2}(f_1 + f_2) - \alpha_2 + ln\left(1 - \frac{\alpha_0}{1+\alpha_s(|u|^2+v^2)}\right), \; D_{yy} = \frac{\alpha_1(1-i\Delta)}{1+\Delta^2}(f_1 - f_2) - \alpha_2 \\
&+ ln\left(1 - \frac{\alpha_0}{1+\alpha_s(|u|^2+v^2)}\right), D_{xy} = D_{yx} = \frac{\alpha_1(1-i\Delta)}{1+\Delta^2}f_3,
\end{aligned}
\tag{4}
$$

where:

$$f_1 = \left(\chi\frac{n_0}{2} - 1\right), f_2 = \chi\frac{n_{12}}{2}, f_3 = \chi\frac{n_{22}}{2}. \tag{5}$$

Here time t is normalized to the photon lifetime in the cavity τ_p, $I_x = /u/^2$, $I_y = /v/^2$ are normalized to the saturation power I_{ss} and I_p is normalized to the saturation power I_{ps}, α_1 is the total absorption of erbium ions at the lasing wavelength; α_2 represents the normalized losses; α_0 and α_s are parameters describing CNT saturable absorber; δ is the ellipticity of the pump wave, $\varepsilon = \tau_p\{/\}\tau_{Er}$ is the ratio of the the photon lifetime in the cavity τ_p to the lifetime of erbium ions at the first excited level τ_{Er}; $\chi_{p,s} = (\sigma_a^{(s,p)} + \sigma_e^{(s,p)})/\sigma_a^{(s,p)}$, $(\sigma_a^{(s,p)}$ and $\sigma_e^{(s,p)}$ are absorption and

emission cross-sections at the lasing (s) and pump (p) wavelengths); Δ is the detuning of the lasing wavelength with respect to the maximum of the gain spectrum (normalized to the gain spectral width), β is the birefringence strength ($2\beta = 2\pi L_c/L_b$, L_b is the beat length and L_c is the cavity length), We use an approximation in Eqs. (3) that the dipole moments of the absorption and emission transitions for erbium-doped silica are located in the plane orthogonal to the direction of the light propagation. This approximation results in the angular distribution of the excited ions $n(\theta)$, which can be expanded into a Fourier series as follows [1,16–19]:

$$n(\theta) = \frac{n_0}{2} + \sum_{k=1}^{\infty} n_{1k} \cos(k\theta) + \sum_{k=1}^{\infty} n_{2k} \sin(k\theta), f_1 = \left(\chi\frac{n_0}{2} - 1\right) + \chi\frac{n_{12}}{2},$$

$$f_2 = \left(\chi\frac{n_0}{2} - 1\right) - \chi\frac{n_{12}}{2}, f_3 = \chi\frac{n_{22}}{2}.$$

(6)

In contrast to more general approximation with 3D orientation distribution of the dipole orientations [20,21], Eqs. (6) results in the finite dimension system presented by Eqs. (3) where only n_0, n_{12}, and n_{21} components contribute to the laser dynamics. Unlike the other vector models, the vector model is in a simpler form presented by Eqs. (3) was justified in our previous publications on the mode-locked laser polarization dynamics at the time scales from one round trip to thousands of round trips [1,16–19].

To obtain results shown in Fig. 4, we used the following parameters: (a), (d), (g) $I_p =25$, $a = 0.001$; (b), (e), (h) $I_p =22$, $a = 0.02$; (c), (f), (i) $I_p =30$, $a = 10$. The other parameters: (a)-(i) $\beta_L = \beta_C = 0$, $\alpha_1 = 5.38$, $\alpha_2 = 1$, $\alpha_s = 10^{-3}$, $\alpha_0 = 0.136$, $\delta = 0.99$ (elliptically polarized pump SOP), $\Delta=0.13$ $\varepsilon=10^{-4}$, $c_p = 1$, $c_s = 2.3$, $\Omega=0.005p$, $f_0 =0$, $Y=p/2$. To model the effect of the output POC transformation caused by the patchcord connect to the polarimeter, we use the following 3D rotation (around axes related to the Stokes parameters S_0, S_1, S_2, S_3) matrix [22]:

$$\begin{pmatrix} \tilde{S}_1 \\ \tilde{S}_2 \\ \tilde{S}_3 \\ \tilde{S}_0 \end{pmatrix} = \begin{bmatrix} a_{11} & a_{12} & a_{13} & 0 \\ a_{21} & a_{22} & a_{23} & 0 \\ a_{31} & a_{32} & a_{33} & 0 \\ 0 & 0 & 0 & 1 \end{bmatrix} \begin{pmatrix} S_1 \\ S_2 \\ S_3 \\ S_0 \end{pmatrix},$$

(7)

$$a_{11} = cos(\psi)cos(\gamma), \ a_{12} = cos(\gamma)sin(\alpha)sin(\psi) - cos(\alpha)sin(\gamma),$$

$$a_{13} = cos(\alpha)cos(\gamma)sin(\psi) + sin(\alpha)sin(\gamma),$$

$$a_{21} = cos(\psi)sin(\gamma), \ a_{22} = cos(\alpha)cos(\gamma) + sin(\alpha)sin(\psi)sin(\gamma),$$

$$a_{23} = -cos(\gamma)sin(\alpha) + sin(\psi)sin(\gamma), \ a_{31} = -sin(\gamma), \ a_{32} = cos(\psi)sin(\alpha),$$

$$a_{33} = cos(\alpha)cos(\psi).$$

As follows from Figs. 4(a)-(h), the injected signal with oscillating SOP modifies the spiral attractor and polarization dynamics of the polarization components x and y. The obtained theoretical results are quite close to the experimental data shown in Figs. 3(a)-(h) that corresponds to the development of the soliton rain's condensed phase in Figs. 2(a), (b). With increasing the amplitude of the injected signal from a = 0.02 to a = 10, the polarization dynamics takes a completely different form, as shown in Figs. 4(c), (f), (i). The spiral attractor is transformed to the circle (Fig. 4 (c)), and x and y components' oscillations take the form of antiphase close to harmonic oscillations with the faster phase difference switching (Figs. 4(f), (i)). The dynamics is quite close to the experimental results shown in Figs. 3(c), (f), (i) and the corresponding emergence of the soliton rain bunch shown in Fig. 2(c).

Our previous publication shows that the mechanism driving the soliton rain origin and merging to the condensate phase is competition between polarization hole burning (PHB) caused by soliton
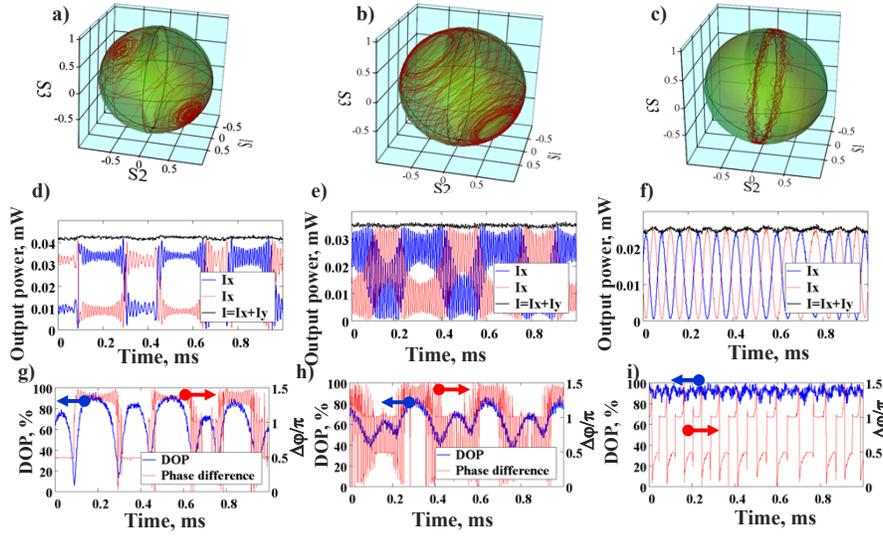
Fig. 3. Slow polarization dynamics: (a)-(c) trajectories on the Poincaré sphere. (d)-(f) The output power vs time for two linearly cross-polarized SOPs I_x (blue line) and I_y (red) and total power $I = I_x + I_y$ (black); (g)-(f) DOP (blue) and the phase difference (red) vs time. Parameters: Pump power P = 114 mW (a), (d), (g); 108 mW (b), (e), (h); 148 mW (c), (f), (i).
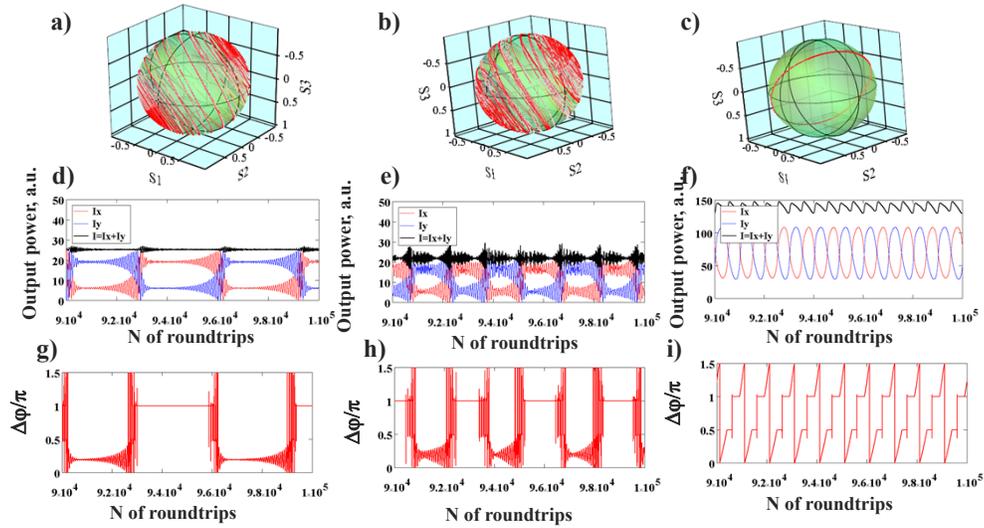
Fig. 4. Slow polarization dynamics: (a)-(c) trajectories on the Poincaré sphere. (d)-(f) The output power vs number of the round trips for two linearly cross-polarized SOPs I_x (blue line) and I_y (red) and total power $I = I_x + I_y$ (black); (g)-(f) the phase difference (red) vs number of the round trips. Parameters: $\alpha = -\pi/4$, $\beta = \pi/4$, $\gamma = 2\pi/5$, (a)-(i); $I_p = 25$ (a), (d), (g); $I_p = 22$ (b), (e), (h); $I_p = 30$ (c), (f), (i). The time span of 10^4 corresponds to 1 ms.

rain pulses and holes refilling by the pump wave [9]. Here we are taking the next step by concluding the effect of the soliton rain on the active medium in modifying the polarization properties. As follows from the Figs. 4(a), (b), (d), (e), (g), (h), the spiral polarization attractor shown in Figs. 3(a), (b), (d), (e), (g), (h) appears when the in-cavity linear and circular birefringence are compensated, i.e., $\beta_L = \beta_C = 0$. The soliton with the evolving state of polarization completely depletes the population inversion. So, soliton rain has a low total power modelled by the injected signal's low power, i.e., a = 0.001 and 0.02 (Figs. 4(a), (b), (d), (e), (g), (h)). Given the low power of the soliton rain, the spiral attractor preserves the shape as shown in Figs. 4(a), (b), (d), (e), (g), (h). With increased pump power from P = 114 mW to 148 mW (Figs. 2 and 3) and from $I_p = 22$ to 30 (Fig. 4), the depleted population inversion is restored by the pump at the fast time scale and so PHB can't deplete the population inversion that results in the CW component's emergence (Fig. 2(f)). Hence, the soliton bunch has an enhanced amplitude and the periodically evolving SOP caused by the bunch drift. As a result, the spiral attractor is transformed into the circle on the Poincaré sphere (Figs. 3(c), (f), (i) and 4 (c), (f), (i)).

5. Conclusion

In conclusion, for the Er-doped fiber laser mode-locked using carbon nanotubes, we have demonstrated experimentally and theoretically that the soliton rain emergence can transform the polarization attractor on Poincaré sphere from spiral to the circle. Such experimentally observed transformation was explained based on the vector model developed by Sergeyev and co-workers in [1,16–19] complemented by the vector SR model in terms of the injected signal with evolving SOP. The evolving SOP mimics the dynamically evolving polarization hole burning in the orientation distribution of Er ions' inversion caused by the main pulses and bunch of drifting soliton rain. The obtained results can pave the wave to development of a new technique for control of the multisoliton supramolecular structure in the form of the soliton rain that of interest for different application including data storage (see Refs. in [14]), spectroscopy [23], metrology [24,25] and biomedical diagnostics [26]. For example, the controllable number of pulses can advance the multi-pulse spectroscopy [23] and distance ranging [24]. Also, the controllable dynamic state of polarization enables the comb laser functionality to detect the object texture [25] or biological tissue malformations [26] based on detecting polarization signatures.

Disclosures. The authors declare no conflicts of interest.

Data availability. Data underlying the results are not publicly available but may be obtained from the authors upon request.

References

1. S. Sergeyev, S. Kolpakov, and Y. Loika, "Vector harmonic mode-locking by acoustic resonance," Photonics Res. **9**(8), 1432 (2021).
2. X. Liu and M. Pang, "Revealing the buildup dynamics of harmonic mode-locking states in ultrafast lasers," Laser Photonics Rev. **13**(9), 1800333 (2019).
3. M. Pang, X. Jiang, W. He, G. K. L. Wong, G. Onishchukov, N. Y. Joly, G. Ahmed, C. R. Menyuk, and P. S. J. Russell, "Stable subpicosecond soliton fiber laser passively mode-locked by gigahertz acoustic resonance in photonic crystal fiber core," Optica **2**(4), 339 (2015).
4. M. Stratmann, T. Pagel, and F. Mitschke, "Experimental observation of temporal soliton molecules," Phys. Rev. Lett. **95**(14), 143902 (2005).
5. Z. Q. Wang, K. Nithyanandan, A. Coillet, P. Tchofo-Dinda, and P. Grelu, "Optical soliton molecular complexes in a passively mode-locked fibre laser," Nat Commun **10**(1), 830 (2019).
6. V. Tsatourian, S. V. Sergeyev, C. Mou, A. Rozhin, V. Mikhailov, B. Rabin, P. S. Westbrook, and S. K. Turitsyn, "Polarisation dynamics of vector soliton molecules in mode locked fibre laser," Sci. Rep. **3**(1), 3154 (2013).
7. R. Weill, A. Bekker, V. Smulakovsky, B. Fischer, and O. Gat, "Noise-mediated Casimir-like pulse interaction mechanism in lasers," Optica **3**(2), 189 (2016).

8. K. Sulimany, O. Lib, G. Masri, A. Klein, M. Fridman, P. Grelu, O. Gat, and H. Steinberg, "Bidirectional soliton rain dynamics induced by casimir-like interactions in a graphene mode-locked fiber laser," Phys. Rev. Lett. **121**(13), 133902 (2018).
9. H. J. Kbashi, S. V. Sergeyev, M. Al Araimi, N. Tarasov, and A. Rozhin, "Vector soliton rain," Laser Phys. Lett. **16**(3), 035103 (2019).
10. S. Chouli and P. Grelu, "Soliton rains in a fiber laser: An experimental study," Phys. Rev. A **81**(6), 063829 (2010).
11. S. Chouli and P. Grelu, "Rains of solitons in a fiber laser," Opt. Express **17**(14), 11776 (2009).
12. A. Niang, F. Amrani, M. Salhi, P. Grelu, and F. Sanchez, "Rains of solitons in a figure-of-eight passively mode-locked fiber laser," Appl. Phys. B **116**(3), 771–775 (2014).
13. H. J. Kbashi, M. Zajnulina, A. G. Martinez, and S. V. Sergeyev, "Mulitiscale spatiotemporal structures in mode-locked fiber lasers," Laser Phys. Lett. **17**(3), 035103 (2020).
14. W. He, M. Pang, D. H. Yeh, J. Huang, C. R. Menyuk, and P. S. J. Russell, "Formation of optical supramolecular structures in a fibre laser by tailoring long-range soliton interactions," Nat Commun **10**(1), 1 (2019).
15. S. V. Sergeyev, H. Kbashi, N. Tarasov, Y. Loiko, and S. A. Kolpakov, "Vector-Resonance-Multimode Instability," Phys. Rev. Lett. **118**(3), 033904 (2017).
16. S. V. Sergeyev, C. Mou, E. G. Turitsyna, A. Rozhin, S. K. Turitsyn, and K. Blow, "Spiral attractor created by vector solitons," Light: Sci. Appl. **3**(1), e131 (2014).
17. S. V. Sergeyev, "Fast and slowly evolving vector solitons in mode-locked fibre lasers," Phil. Trans. R. Soc. A **372**(2027), 20140006 (2014).
18. S. V. Sergeyev, "Vector self-pulsing in erbium-doped fiber lasers," Opt. Lett. **41**(20), 4700 (2016).
19. H. Zeghlache and A. Boulnois, "Model and steady states of neodymium-doped fiber lasers," Phys. Rev. A **52**(5), 4229–4242 (1995).
20. S. V. Sergeyev, "Spontaneous light-polarization symmetry breaking for an anisotropic ring-cavity dye laser," Phys. Rev. A **59**(5), 3909–3917 (1999).
21. V. A. Gaisenok, G. G. Krylov, and S. V. Sergeyev, "Dynamic operations of a dye laser with a saturable absorber: pumping anisotropy and orientational relaxation," Physica D **72**(1-2), 161–165 (1994).
22. D. A. Varshalovich, A. N. Moskalev, and V. K. Khersonskii, *Quantum Theory of Angular Momentum* (World Scientific, 1988), 21–23.
23. R. Yang, H. Sun, H. Lv, J. Xu, J. Wu, P. Hu, H. Fu, H. Yang, and J. Tan, "A Multidimensional Multiplexing Mode-Locked Laser Based on a Dual-Ring Integrative Structure for Tri-Comb Generation," Appl. Sci. **10**(22), 8260 (2020).
24. S. Zhou, C. Lin, Y. Yang, and G. Wu, "Multi-pulse sampling dual-comb ranging method," Opt. Express **28**(3), 4058 (2020).
25. S. V. Sergeyev and S. Turitsyn, "Systems and methods for measuring a distance to a target and the complex reflectance ratio of a target," WO/2020/039039.
26. M. Kupinski, M. Boffety, F. Goudail, R. Ossikovski, A. Pierangelo, J. Rehbinder, J. Vizet, and T. Novikova, "Polarimetric Measurement Utility for Pre-cancer Detection from Uterine Cervix Specimens," Biomed. Opt. Express **9**(11), 5691–5702 (2018).